

# RECONSTRUCTING CONDUCTIVITIES WITH BOUNDARY CORRECTED D-BAR METHOD

SAMULI SILTANEN AND JANNE P. TAMMINEN

**ABSTRACT.** The aim of electrical impedance tomography is to form an image of the conductivity distribution inside an unknown body using electric boundary measurements. The computation of the image from measurement data is a non-linear ill-posed inverse problem and calls for a special regularized algorithm. One such algorithm, the so-called D-bar method, is improved in this work by introducing new computational steps that remove the so far necessary requirement that the conductivity should be constant near the boundary. The numerical experiments presented suggest two conclusions. First, for most conductivities arising in medical imaging, it seems the previous approach of using a best possible constant near the boundary is sufficient. Second, for conductivities that have high contrast features at the boundary, the new approach produces reconstructions with smaller quantitative error and with better visual quality.

## 1. INTRODUCTION

The aim of electrical impedance tomography (EIT) is to form an image of the conductivity distribution inside an unknown body using electric boundary measurements. Applications of EIT include medical imaging, nondestructive testing and subsurface monitoring. See [16] for an overview of EIT. The computation of the image from measurement data is a non-linear ill-posed inverse problem and calls for a special regularized algorithm. In this work we improve one such algorithm, the so-called D-bar method, by removing the so far necessary requirement that the conductivity should be constant near the boundary.

The mathematical model behind EIT is the *inverse conductivity problem* introduced by Calderón in [14]. We discuss here the inverse conductivity problem in the following two-dimensional form: let  $\Omega_1 = D(0, r_1) \subset \mathbb{R}^2$  be the disc with center at origin and radius  $r_1 > 0$  and consider a strictly positive, real-valued conductivity  $\sigma \in C^2(\overline{\Omega}_1)$ . Maintaining a voltage distribution  $f$  on the boundary  $\partial\Omega_1$  creates a voltage potential  $u$  that solves the following Dirichlet problem:

$$(1) \quad \begin{cases} \nabla \cdot (\sigma \nabla u) &= 0 & \text{in } \Omega_1, \\ u &= f & \text{on } \partial\Omega_1. \end{cases}$$

The resulting distribution of current through the boundary is

$$(2) \quad \Lambda_\sigma f = \sigma \frac{\partial u}{\partial \nu} \Big|_{\partial\Omega_1}$$

where  $\nu$  is the outward unit normal and  $\Lambda_\sigma$  is the Dirichlet-to-Neumann (DN) map. Calderón's problem is to reconstruct  $\sigma$  from the knowledge of  $\Lambda_\sigma$ .

Many numerical methods have been suggested in the literature for the reconstruction of  $\sigma$  in the above setting. In this work we concentrate on the so-called

D-bar method. Other approaches include linearization [5, 8, 17], iterative regularization [20, 21, 37, 26], statistical inversion [25, 45], resistor network methods [11], convexification [47], layer stripping [49, 50] and Teichmüller space methods [34, 35, 36]. Also, there is a large body of work concentrating on recovering partial information on  $\sigma$ , see [9, 10] for a survey.

Theoretical foundation of the D-bar method for EIT in dimension two was introduced by Nachman in [42], where a constructive proof for recovering  $\sigma \in W^{2,p}(\Omega_1)$  from  $\Lambda_\sigma$  was given for  $p > 1$ . The result was later sharpened by Brown and Uhlmann [13] to cover  $W^{1,q}(\Omega_1)$  conductivities with  $q > 2$ ; the proof was augmented with constructive steps by Knudsen and Tamasan in [29]. Finally, Astala and Päiväranta answered Calderón's question in its original form by describing a constructive procedure for recovering  $\sigma \in L^\infty(\Omega_1)$  in [3, 4]; numerical implementation of this approach is described in [1, 2]. Thus there are several variants of the D-bar method for two-dimensional EIT. In dimension three, the theory of D-bar reconstruction is developed in [19, 41, 44, 51, 7].

The above theoretical results on the D-bar method assume the knowledge of the infinite-precision data  $\Lambda_\sigma$ . However, the starting point of practical inversion is a finite-dimensional and noisy approximation  $L_\sigma^\varepsilon$  to  $\Lambda_\sigma$ . Since the EIT problem is severely ill-posed, or sensitive to measurement noise, any practical reconstruction method needs to be robust against errors in measurement data. The first robust D-bar algorithm (based on [42]) was given in [48], and it has been refined and analysed in [38, 30, 31, 32]. The method has been successfully tested on a chest phantom in [23] and on *in vivo* human chest data in [24]. Numerical D-bar method based on [13, 29] was reported in [28]. The above methods are two-dimensional; three-dimensional computations are described in [6, 12]. Robustness is ensured in all of these practical D-bar reconstruction methods by truncating scattering data, a step that can be viewed as nonlinear low-pass filtering.

In addition to being robust against noise, a reliable EIT algorithm needs a regularization analysis. Such an analysis is provided for the two-dimensional D-bar method in [33], where an explicit formula is given for choosing the truncation radius as function of noise level.

Practical D-bar methods have been until now implemented by fitting an optimal constant to the possibly nonconstant trace  $\sigma|_{\partial\Omega_1}$ . Quite good results have been obtained both with laboratory data [23] and *in vivo* patient data [24]. However, in applications exhibiting large conductivity changes near or at the boundary the constant-fitting approach may not be good enough. Our aim here is to remove the assumption " $\sigma \equiv 1$  near the boundary" from the two-dimensional D-bar algorithm based on [42] using an additional procedure we call *boundary correction*.

Let us review the infinite-precision boundary correction procedure given in [42]. The starting point is the DN map  $\Lambda_\sigma$  of a conductivity  $\sigma \in W^{2,p}(\Omega_1)$ . Take  $r_2 > r_1$  and set  $\Omega_2 = D(0, r_2)$ . The conductivity  $\sigma$  is extended outside  $\Omega_1$  by

$$(3) \quad \gamma(x) = \begin{cases} \sigma(x), & \text{when } x \in \Omega_1, \\ \tilde{\sigma}(x), & \text{when } x \in \Omega_2 \setminus \overline{\Omega_1}, \end{cases}$$

where we can choose any  $\tilde{\sigma} \in W^{2,p}(\Omega_2 \setminus \overline{\Omega_1})$  with the properties  $\tilde{\sigma}|_{\partial\Omega_1} = \sigma|_{\partial\Omega_1}$  and  $(\partial\sigma/\partial\nu)|_{\partial\Omega_1} = (\partial\tilde{\sigma}/\partial\nu)|_{\partial\Omega_1}$  and  $\tilde{\sigma} \equiv 1$  near  $\partial\Omega_2$ . This way  $\gamma \in W^{2,p}(\Omega_2)$  whenever

$\sigma \in W^{2,p}(\Omega_1)$ . Define two Dirichlet problems:

$$(4) \quad \begin{cases} \nabla \cdot (\tilde{\sigma} \nabla u_j) &= 0 & \text{in } \Omega_2 \setminus \overline{\Omega_1}, \quad j = 1, 2 \\ u_j &= f_j & \text{on } \partial\Omega_j \\ u_j &= 0 & \text{on } \partial\Omega_i, \quad i = 1, 2, \quad i \neq j. \end{cases}$$

Four new DN maps in  $\Omega_2 \setminus \overline{\Omega_1}$  can be defined by

$$(5) \quad \Lambda^{ij} f_j = \tilde{\sigma} \frac{\partial u_j}{\partial \nu} \Big|_{\partial\Omega_i}, \quad i, j = 1, 2.$$

By proposition 6.1 of [42] we can use (5) to write  $\Lambda_\gamma$  in terms of  $\Lambda_\sigma$ :

$$(6) \quad \Lambda_\gamma = \Lambda^{22} + \Lambda^{21}(\Lambda_\sigma - \Lambda^{11})^{-1} \Lambda^{12}.$$

The boundary corrected D-bar method for  $\sigma \in W^{2,p}(\Omega_1)$ , assuming infinite-precision data, is described as follows in [42, Section 6]:

- (a) **Reconstruction at the boundary.** Recover the trace  $\sigma|_{\partial\Omega_1}$  and the normal derivative  $(\partial\sigma/\partial\nu)|_{\partial\Omega_1}$  from  $\Lambda_\sigma$ .
- (b) **Extension of conductivity.** Using (a) and (3), extend the conductivity to  $\gamma \in W^{2,p}(\Omega_2)$  such that  $\gamma \equiv 1$  near  $\partial\Omega_2$  and  $\inf_{x \in \Omega_2} \gamma(x) \geq c > 0$ ;
- (c) **Calculation of outer DN map.** Write the DN map  $\Lambda_\gamma$  of  $\gamma \in W^{2,p}(\Omega_2)$  in terms of  $\Lambda_\sigma$  using (6);
- (d) **Reconstruction using the D-bar method.** Reconstruct  $\gamma \in W^{2,p}(\Omega_2)$  from the infinite-precision data  $\Lambda_\gamma$  following [42].

The practical starting point of reconstruction is the noisy approximate data  $L_\sigma^\varepsilon$ , and the Steps (a–d) above cannot be directly followed. We suggest the following robust procedure for boundary correction:

- (a') **Approximate reconstruction at the boundary.** Recover numerically a smooth function  $g \in C^\infty(\partial\Omega_1)$  with the property  $g \approx \sigma|_{\partial\Omega_1}$  as explained in [43]. Omit recovering  $(\partial\sigma/\partial\nu)|_{\partial\Omega_1}$  since it is an unstable step [43];
- (b') **Simple extension of conductivity.** Construct  $\tilde{\sigma} \in C^2(\overline{\Omega_2 \setminus \Omega_1})$  satisfying  $\inf_{x \in \Omega_2 \setminus \overline{\Omega_1}} \tilde{\sigma}(x) \geq c > 0$  and  $\tilde{\sigma}|_{\partial\Omega_1} = g$  and  $\tilde{\sigma} \equiv 1$  near  $\partial\Omega_2$ . Use  $\tilde{\sigma}$  in (3) to extend the conductivity to  $\gamma \in L^\infty(\Omega_2)$ ;
- (c') **Approximate calculation of outer DN map.** Write approximate DN map  $L_\gamma$  in terms of  $L_\sigma$  using a matrix approximation to (6);
- (d') **Reconstruction using regularized D-bar method.** Reconstruct  $\gamma$  from  $L_\gamma$  using the regularized D-bar method described in [33].

The main concern about the procedure (a'–d') is that the extension of  $\sigma$  to  $\gamma$  will be in general discontinuous at  $\partial\Omega_1$ , and thus  $\gamma$  violates the assumptions of the D-bar method used in (d'). However, there is both theoretical and experimental evidence suggesting that the step (d') should give reasonable results even in this case [23,

24, 32, 31]. Another potential problem arises from the inverse operator in formula (6), as the proof of invertibility [42, Proposition 6.1] in the extended conductivity produced by step (b'). One possibility would be to use [27, Lemma 2.1.3.] instead of (6) as the basis of step (b'). However, in our computational experiments the use of (6) seems not to be a problem even in the case of discontinuous conductivity extensions.

This paper should be viewed as a report of computational experiments suggesting the practical usefulness of the boundary correction step in applications where the conductivity varies strongly near the boundary. Hopefully the computational results presented below will act as motivation for further theoretical study of practical imaging algorithms for EIT.

We remark that the boundary correction method is applied in this paper only in the case of  $\Omega_1$  being a disc. This is not a serious lack of generality, though: we presume that other domains than discs could be treated combining the methods described in [39, 40] with the boundary correction.

This paper is organized as follows. We present our method of simulating continuum model EIT data in Section 2. The details of implementation of Steps (a') and (b') and (c') are discussed in Sections 3 and 4 and 5, respectively. A brief outline of the regularized D-bar method is given in Section 6. Our practical boundary correction method is illustrated by numerical examples in Section 7, and we conclude our results in Section 8.

## 2. SIMULATION OF MEASUREMENT DATA

Let  $\mathcal{R}_\sigma : \tilde{H}^{-1/2}(\partial\Omega_1) \rightarrow \tilde{H}^{1/2}(\partial\Omega_1)$  denote the Neumann-to-Dirichlet map of  $\sigma$ , where  $\tilde{H}^s$  spaces consist of  $H^s$  functions with mean value zero. We have  $\mathcal{R}_\sigma g = u|_{\partial\Omega_1}$ , where  $u$  is the unique  $H^1(\Omega_1)$  solution of the Neumann problem

$$\nabla \cdot \sigma \nabla u = 0 \text{ in } \Omega_1, \quad \gamma \frac{\partial u}{\partial \nu} = g \text{ on } \partial\Omega_1,$$

satisfying  $\int_{\partial\Omega_1} u ds = 0$ . We note two key equalities concerning  $\Lambda_\sigma$  and  $\mathcal{R}_\sigma$ . Define a projection operator  $P\phi := |\partial\Omega_1|^{-1} \int_{\partial\Omega_1} \phi$ . Then for any  $f \in H^{1/2}(\partial\Omega_1)$  we have  $P\Lambda_\sigma f = |\partial\Omega_1|^{-1} \int_{\partial\Omega_1} \sigma \frac{\partial u}{\partial \nu} = \int_{\Omega_1} \nabla \cdot \sigma \nabla u = 0$ , so actually  $\Lambda_\sigma : H^{1/2}(\partial\Omega_1) \rightarrow \tilde{H}^{-1/2}(\partial\Omega_1)$ . From the definitions of  $\Lambda_\sigma$  and  $\mathcal{R}_\sigma$  we now have

$$(7) \quad \Lambda_\sigma \mathcal{R}_\sigma = I \quad : \tilde{H}^{-1/2}(\partial\Omega_1) \rightarrow \tilde{H}^{-1/2}(\partial\Omega_1),$$

$$(8) \quad \mathcal{R}_\sigma \Lambda_\sigma = I - P \quad : H^{1/2}(\partial\Omega_1) \rightarrow \tilde{H}^{1/2}(\partial\Omega_1).$$

Given  $\sigma$  and  $N > 0$ , we define a matrix  $R_\sigma : \mathbb{C}^{2N} \rightarrow \mathbb{C}^{2N}$  as follows. We use a truncated orthonormal trigonometric basis for representing functions defined at the boundary  $\partial\Omega_j$ :

$$(9) \quad \phi_j^{(n)}(\theta) = \frac{1}{\sqrt{2\pi r_j}} e^{in\theta}, \quad n = -N, \dots, N, \quad j = 1, 2.$$

Note that  $\int_{\partial\Omega_j} \phi_j^{(n)} ds = 0$  for  $n \neq 0$ . Then solve the Neumann problem

$$(10) \quad \nabla \cdot \sigma \nabla u_1^{(n)} = 0 \text{ in } \Omega_1, \quad \sigma \frac{\partial u_1^{(n)}}{\partial \nu} = \phi_1^{(n)} \text{ on } \partial\Omega_1,$$

with the constraint  $\int_{\partial\Omega_1} u_1^{(n)} ds = 0$ . Define  $R_\sigma = [\hat{u}(\ell, n)]$  by

$$(11) \quad \hat{u}(\ell, n) = \int_{\partial\Omega_1} u_1^{(n)} \overline{\phi_1^{(\ell)}} ds.$$

Here  $\ell$  is the row index and  $n$  is the column index.

The matrix  $R_\sigma$  represents the operator  $\mathcal{R}_\sigma$  approximately. We add simulated measurement noise by defining

$$(12) \quad R_\sigma^\varepsilon := R_\sigma + cE,$$

where  $E$  is a  $2N \times 2N$  matrix with random entries independently distributed according to the Gaussian normal density  $\mathcal{N}(0, 1)$ . The constant  $c > 0$  is adjusted so that  $\|R_1^\varepsilon - R_1\|/\|R_1\|$ , where  $\|\cdot\|$  is the standard matrix norm and  $R_1$  is the ND-map for the unit conductivity, is greater than the relative error caused by FEM and of the same order of magnitude as 0.0017% (signal to noise -ratio of 95.5 dB), the noise level of the ACT3 impedance tomography imager of Rensselaer Polytechnic Institute [18].

We can now easily compute the corresponding noisy matrix representation  $L_\sigma^\varepsilon$  for the DN map  $\Lambda_\sigma$ . Namely, define

$$\widetilde{L}_\sigma^\varepsilon := (R_\sigma^\varepsilon)^{-1};$$

then  $\widetilde{L}_\sigma^\varepsilon$  is a matrix of size  $2N \times 2N$ . We should add appropriate mapping properties for constant basis functions at the boundary according to the facts

$$\Lambda_\sigma 1 = 0, \quad \int_{\partial\Omega_1} \Lambda_\sigma f ds = 0.$$

This is achieved simply by setting (in Matlab notation)

$$(13) \quad L_\sigma^\varepsilon := \begin{bmatrix} \widetilde{L}_\sigma^\varepsilon(1:N, 1:N) & 0 & \widetilde{L}_\sigma^\varepsilon(1:N, (N+1):\text{end}) \\ 0 & 0 & 0 \\ \widetilde{L}_\sigma^\varepsilon((N+1):\text{end}, 1:N) & 0 & \widetilde{L}_\sigma^\varepsilon((N+1):\text{end}, (N+1):\text{end}) \end{bmatrix},$$

where the zero block matrices above have various (but obvious) sizes.

### 3. APPROXIMATE RECONSTRUCTION AT THE BOUNDARY

The trace  $\sigma|_{\partial\Omega_1}$  can be approximately reconstructed in the following way [43]. Define  $h_{M,\beta}(\theta) = e^{iM\theta}\eta(\theta - \beta)$ , where

$$(14) \quad \eta(\theta) = \begin{cases} d(\kappa\theta - \pi/2)^\alpha (\kappa\theta + \pi/2)^\alpha \cos(\kappa\theta), & \text{for } -\pi/(2\kappa) < \theta < \pi/(2\kappa), \\ 0, & \text{otherwise} \end{cases}$$

is a non-negative cut-off function satisfying  $\int_{\partial\Omega_1} \eta^2(\theta) d\theta = 1$ . Now the mollified trace  $(\sigma\eta^2)|_{\partial\Omega_1}(\beta)$  can be calculated with

$$(15) \quad \int_{\partial\Omega_1} \sigma\eta^2 ds = \lim_{M \rightarrow \infty} \frac{1}{M} \int_{\partial\Omega_1} \overline{h_{M,\beta}} \Lambda_\sigma h_{M,\beta} ds.$$

We get the approximation  $g \approx \sigma|_{\partial\Omega_1}$  by calculating (15) with different angles  $\beta$  and using a finite  $M$  in the right side of (15).

Another approach to reconstructing  $\sigma|_{\partial\Omega_1}$  is the layer stripping method introduced in [49].

#### 4. SIMPLE EXTENSION OF CONDUCTIVITY

The starting point here is a given approximation  $g : \partial\Omega_1 \rightarrow \mathbb{R}$  to the trace  $\sigma|_{\partial\Omega_1}$  of the conductivity  $\sigma \in C^2(\overline{\Omega_1})$  of interest. The aim is to construct a strictly positive conductivity  $\tilde{\sigma} : \Omega_2 \setminus \overline{\Omega_1}$  satisfying  $\tilde{\sigma}|_{\partial\Omega_1} = g$  and  $\tilde{\sigma} \equiv 1$  near the outer boundary  $\partial\Omega_2$ , and then use formula (3) to define  $\gamma$ .

We extend  $\sigma$  to  $\gamma$  using the following extension in polar coordinates:

$$(16) \quad \gamma(\rho, \theta) = \begin{cases} \sigma(\rho, \theta), & \rho \leq r_1, \\ (g(\theta) - 1)f_m(\rho) + 1, & r_1 < \rho \leq r_e, \\ 1, & r_e < \rho \leq r_2, \end{cases}$$

where  $r_1 < r_e < r_2$  is some radius and  $f_m(\rho) \geq 0$  is a suitable third-degree polynomial satisfying  $f_m(r_1) = 1$  and  $f_m(r_e) = 0$ . Note that  $\gamma$  is twice continuously differentiable apart from possible discontinuity at  $\rho = r_1$ , and equals constant 1 in the annulus  $r_e < \rho < r_2$ .

#### 5. APPROXIMATE CALCULATION OF OUTER DN MAP

Using the functions (9), a given function  $f : \partial\Omega_i \rightarrow \mathbb{C}$  can be approximately represented by the vector

$$\vec{f} = [\hat{f}(-N), \hat{f}(-N+1), \dots, \hat{f}(N-1), \hat{f}(N)]^T, \quad \hat{f}(n) = \int_{\partial\Omega_i} f \overline{\phi_i^{(n)}} ds,$$

and the DN maps  $\Lambda^{ij}$  can be approximated by the matrices  $L^{ij} = [\hat{g}_{ij}(\ell, n)]$  with

$$(17) \quad \hat{g}_{ij}(\ell, n) = \int_{\partial\Omega_j} \tilde{\sigma} \frac{\partial u_j^{(n)}}{\partial \nu} |_{\partial\Omega_i} \overline{\phi_j^{(\ell)}} dS,$$

where  $u_j^{(n)}$  denotes the solution to (4) with  $u_j^{(n)}|_{\partial\Omega_j} = \phi_j^{(n)}$ . Again  $\ell$  is the row index and  $n$  is the column index. Now the matrix  $L_\gamma^\varepsilon$  can be calculated by

$$(18) \quad L_\gamma^\varepsilon = L^{22} + L^{21}(L_\sigma^\varepsilon - L^{11})^{-1}L^{12},$$

provided that the matrix  $L_\sigma^\varepsilon - L^{11}$  is invertible. Formula (18) is a finite-dimensional approximation to (6).

#### 6. REGULARIZED D-BAR METHOD

In this section we explain how to reconstruct a conductivity  $\gamma$  in a regularized way from a noisy measurement matrix  $L_\gamma^\varepsilon$  under the assumptions  $\gamma \in C^2(\overline{\Omega_2})$  and  $\gamma \equiv 1$  in a neighborhood of  $\partial\Omega_2$ .

If we had the infinite-precision data  $\Lambda_\gamma$  at our disposal, we could follow the reconstruction procedure in [42]. First we would solve the boundary integral equation

$$(19) \quad \psi(\cdot, k)|_{\partial\Omega_2} = e^{ikx} - S_k(\Lambda_\gamma - \Lambda_1)\psi(\cdot, k)|_{\partial\Omega_2},$$

in the Sobolev space  $H^{1/2}(\partial\Omega_2)$  for all  $k \in \mathbb{C} \setminus \{0\}$ . In formula (19),  $S_k$  is a single-layer operator

$$(S_k\phi)(x) := \int_{\partial\Omega_2} G_k(x-y)\phi(y)ds,$$

where  $G_k$  is Faddeev's Green function defined by

$$G_k(x) := e^{ikx} g_k(x), \quad g_k(x) := \frac{1}{(2\pi)^2} \int_{\mathbb{R}^2} \frac{e^{ix \cdot \xi}}{|\xi|^2 + 2k(\xi_1 + i\xi_2)} d\xi.$$

Once equation (19) had been solved, we would substitute the result into

$$(20) \quad \mathbf{t}(k) = \int_{\partial\Omega_2} e^{i\bar{k}\bar{x}} (\Lambda_\gamma - \Lambda_1) \psi(\cdot, k) ds,$$

where  $\mathbf{t}$  is called the scattering transform, and  $\Lambda_1$  is the DN map for the unit conductivity. For each fixed  $x \in \Omega$ , we would solve the following integral formulation of the D-bar equation:

$$(21) \quad \mu(x, k) = 1 + \frac{1}{(2\pi)^2} \int_{\mathbb{R}^2} \frac{\mathbf{t}(k')}{(k - k')\bar{k}'} e^{i(k'x + \bar{k}'\bar{x})} \overline{\mu(x, k')} dk'_1 dk'_2;$$

then the conductivity would be perfectly reconstructed as  $\gamma(x) = \mu(x, 0)^2$ .

However, since our starting point in practice is the matrix  $L_\gamma^\varepsilon$ , we need to regularize the above ideal approach as explained in [33]. The matrices  $L_\gamma^\varepsilon$  and  $L_1$  we already have, and a matrix representation  $\mathbf{S}_k$  for the single-layer operator  $S_k$  can be computed numerically, provided we have numerical evaluation routines for  $g_k(x)$ , see [22]. We expand  $e^{ikx}|_{\partial\Omega_2}$  as a vector  $\vec{g}$  in our finite trigonometric basis (9) and set

$$(22) \quad \vec{\psi}_k := [I + \mathbf{S}_k(L_\gamma^\varepsilon - L_1)]^{-1} \vec{g}.$$

for  $k$  ranging in a fine grid inside the disc  $|k| < R$ , where the truncation radius  $R > 0$  is ideally chosen according to the size of noise. The choice of  $R$  falls outside the scope of this paper, so we will compute below reconstructions with  $R$  ranging in an interval. We define the truncated scattering transform by

$$(23) \quad \mathbf{t}_R(k) = \begin{cases} \int_{\partial\Omega_2} e^{i\bar{k}\bar{x}} \mathcal{F}^{-1}((L_\gamma^\varepsilon - L_1)\vec{\psi}_k)(x) ds & \text{for } |k| < R, \\ 0, & \text{otherwise,} \end{cases}$$

where  $\mathcal{F}^{-1}$  denotes transforming from the Fourier series domain to the function domain. Finally we use the numerical algorithm in [30] to solve equation (21) with  $\mathbf{t}$  replaced by  $\mathbf{t}_R$  and denote the solution by  $\mu_R(x, k)$ . Then  $\gamma(x) \approx \mu_R(x, 0)^2$ .

## 7. NUMERICAL RESULTS

We define several conductivity distributions  $\sigma \in L^\infty(\Omega_1)$  on the unit disc  $\Omega_1 = D(0, r_1) = D(0, 1)$  and compare reconstructions computed with and without the boundary correction procedure.

Before proceeding with the examples, though, we need to choose an optimal radius  $r_2$  to be used in the boundary correction step. We do this by examining numerically the simple case of the unit conductivity  $\sigma \equiv 1$  and using the procedure (a'-c') explained in the introduction. The numerical parameters used in this procedure are the same as in the example reconstructions, and they are given later in this chapter.

We take  $N = 16$  and simulate non-noisy ND map  $R_1$  using the finite element method with 1048576 triangles in  $\Omega_1$  as explained in Section 2. Using the standard square norm for matrices, this yields  $\epsilon_{\text{fem}} = \|R_1^{\text{th}} - R_1\|/\|R_1^{\text{th}}\| \approx 0.0000173$ , where  $R_1^{\text{th}}$  is the analytically calculated ND matrix for the unit conductivity. Furthermore,

we construct noisy ND map  $R_1^\epsilon$  with formula (12) and  $c = 0.00001$ , giving  $\|R_1^\epsilon - R_1\|/\|R_1\| \approx 0.0001 > \epsilon_{\text{fem}}$ .

To avoid notational clashes, we denote by

- $L_{\gamma=1}^\epsilon$  the DN map on  $\partial\Omega_2$  computed from noisy ND map using formula (18),
- $L_{\gamma=1}$  the DN map computed from non-noisy ND map using formula (18),
- $L_{\gamma=1}^2$  the DN map computed directly on  $\partial\Omega_2$ ,

where by  $\gamma = 1$  we mean the conductivity  $\sigma = 1$  extended by (16). The left plot in Figure 1 shows the behaviour of the error  $\|L_{\gamma=1}^\epsilon - L_{\gamma=1}^2\|/\|L_{\gamma=1}^2\|$  as a function of  $r_2$ . The condition number of the matrix  $L_{\sigma=1}^\epsilon - L^{11}$  ranges between 1 and 20. It seems that we should choose  $r_2 \geq 1.2$ . Further, the right plot in Figure 1 shows the behaviour of the error  $\|L_{\gamma=1}^\epsilon - L_{\gamma=1}\|/\|L_{\gamma=1}\|$  as function of  $r_2$ . The error decreases as  $r_2$  grows; it shows how the data measured on  $\partial\Omega_1$  contributes less and less to  $L_{\gamma=1}^\epsilon$  as  $r_2$  gets larger. This observation is in agreement with the known fact that in EIT it is more difficult to obtain information from the deeper parts of the object [15].

Based on the above numerical investigation we choose  $r_2 = 1.2$  for the rest of this paper. We work with the following four example conductivities:

- Example one: conductivity has a high contrast bump right on the boundary  $\partial\Omega_1$  and a circular inclusion near the boundary. All deviations from background conductivity 1 satisfy  $\sigma(x) > 1$ .
- Example two: similar to Example one but with a larger inclusion having higher conductivity.
- Example three: conductivity has high-contrast behaviour near  $\partial\Omega_1$ , but the maximum of the deviation from background is not right at the boundary.
- Example four: crude model of a cross-section of an industrial pipeline, similar to the case in [46]. There is a sediment layer on the bottom of the tube, and two round low-conductivity inclusions.

See Figure 2 for plots of the example conductivities and their traces on  $\partial\Omega_1$ .

We simulate noisy EIT data for each example conductivity using  $c = 0.00001$ . The error  $\|R_\sigma^\epsilon - R_\sigma\|/\|R_\sigma\|$  ranges between 0.00011 and 0.00076.

We use the method of Section 3 with  $M = 32, \kappa = 6, \alpha = 4$  and 100 different angles to compute approximately reconstructed traces  $g$  on  $\partial\Omega_1$ . See the right column of Figure 2 for the result. Then, we compute the extended conductivity  $\gamma$  in the disc  $\Omega_2 = D(0, r_2) = D(0, 1.2)$  using (16) and (3) with the radius  $r_e = r_1 + 7/8(r_2 - r_1) = 1.175$ . Since  $g$  is only approximately the same as  $\sigma|_{\partial\Omega_1}$  there are discontinuities in  $\gamma$  in all cases.

We compute the intermediate DN maps  $\Lambda^{ij}$  using the finite element method and 425984 triangles in the annulus  $\Omega_2 \setminus \overline{\Omega_1}$ . To check the accuracy of formula (18) we also calculate  $\Lambda_\gamma$  directly by the finite element method (and 1081344 triangles in  $\Omega_2$ ) using the knowledge of  $\gamma$ . The error  $\|L_\gamma^\epsilon - L_\gamma^2\|/\|L_\gamma^2\|$ , where  $L_\gamma^2$  is the DN map calculated directly on the boundary  $\partial\Omega_2$ , was less than 2.2% in all cases. The condition number of the matrix  $L_\sigma^\epsilon - L^{11}$  used in (18) was less than 27 in all test cases.

Figure 3 illustrates how the noise and the boundary correction procedure affect the scattering transform in example four. The first row shows the real and imaginary parts of (23) substituting  $L_\sigma$  in place of  $L_\sigma^\epsilon$ . The second row shows the same functions using  $L_\sigma^\epsilon$ , and the third row is again the same, but uses  $L_\gamma^\epsilon$  calculated

from (18). The real part of  $\mathbf{t}_R(k)$  is in the left column, the imaginary part on the right. The scattering transform is calculated in a grid of spectral parameters  $k$ , where  $|k| < 10$ . In white areas we have  $|\mathbf{t}_R(k)| > 15$ , meaning the calculation has failed or is close to failing due to computational error caused by large values of  $|k|$ .

For all truncation radii  $R = 3.0, 3.2, \dots, 5.8, 6.0$ , as explained in Section 6, a reconstruction is calculated with and without the boundary correction procedure using the same reconstruction points. The conductivities and their extensions are pictured in figure 2. Full error graph showing  $L^2$ -error for every reconstruction is pictured in figure 4. Reconstructions and the corresponding errors are pictured in figures 5, 6, 7 and 8. The first reconstruction pair is always calculated with  $R = 3$ , the second one is the one with the lowest numerical  $L^2$ -error for the boundary corrected reconstruction, and the third one is with  $R = 6$  to show how the reconstructions fail.

## 8. CONCLUSION

Our aim in this work is to find examples of simulated conductivities that (i) share features of conductivities appearing in applications of electrical impedance tomography, and (ii) allow higher-quality reconstruction when boundary correction step is added to the D-bar method. After experimenting with a large number of candidate conductivities we concluded that for conductivities which behave moderately at and near  $\partial\Omega_1$ , the method of approximating the trace of conductivity by an optimal constant is good enough. More precisely, the errors caused by measurement noise in Steps (a') and (c') prevented the boundary correction procedure from enhancing the reconstructions.

However, we were able to find several examples where the boundary corrected D-bar method does provide better imaging quality than the non-corrected method both in terms of quantitative error and visual inspection. Four such examples are presented in Section 7, and all of them have high contrast features in the conductivity right at the boundary. Consequently, most medical applications do not need the boundary correction procedure, but it may be beneficial or even necessary for some nondestructive testing, industrial process monitoring or geophysical sensing applications.

## ACKNOWLEDGMENTS

During part of the preparation of this work, SS worked as professor and JT worked as an assistant at the Department of Mathematics of Tampere University of Technology. The research work of both authors was funded in part by the Finnish Centre of Excellence in Inverse Problems Research (Academy of Finland CoE-project 213476). The authors thank Jennifer Mueller for her valuable comments on the manuscript. JT was supported in part by Pirkanmaan kulttuurirahasto.

## REFERENCES

- [1] Astala K, Mueller J L, Perämäki A, Päivärinta L and Siltanen S, Direct electrical impedance tomography for nonsmooth conductivities. To appear in *Inverse Problems and Imaging*.
- [2] Astala K, Mueller J L, Päivärinta L and Siltanen S 2010, Numerical computation of complex geometrical optics solutions to the conductivity equation. *Applied and Computational Harmonic Analysis* 29, pp. 2-17.
- [3] K. Astala and L. Päivärinta, *Calderón's inverse conductivity problem in the plane*, *Ann. of Math.*, **163** (2006), 265–299.

- [4] K. Astala and L. Päiväranta, *A boundary integral equation for Calderón's inverse conductivity problem*, Coll. Math. 2006, **Vol. Extra**, 127–139.
- [5] D. C. Barber and B. H. Brown, *Applied potential tomography*, J. Phys. E. Sci. Instrum, **17** (1984), 723–733.
- [6] J. Bikowski, *Electrical Impedance Tomography reconstructions in two and three dimensions; From Calderón to Direct Methods*, Ph.D thesis, Colorado State University, 2008.
- [7] J. Bikowski, K. Knudsen, J. L. Mueller, *Direct numerical reconstruction of conductivities in three dimensions using scattering transforms*, Inverse Problems **27**, 015002
- [8] J. Bikowski and J. L. Mueller, *2D EIT reconstructions using Calderón's method*, Inverse Problems and Imaging, **2** (2008), 43–61.
- [9] L. Borcea, *Electrical Impedance Tomography*, Inverse Problems, **18** (2002), R99–R136.
- [10] L. Borcea, *Addendum to Electrical Impedance Tomography*, Inverse Problems, **19** (2003), 997–998.
- [11] L. Borcea, V. Druskin and F. G. Vazquez, *Electrical impedance tomography with resistor networks*, Inverse Problems, **24** (2008), 31 pp.
- [12] G. Boverman, D. Isaacson, T.-J. Kao, G. J. Saulnier and J. C. Newell, *Methods for Direct Image Reconstruction for EIT in Two and Three Dimensions*, Proceedings of the 2008 Electrical Impedance Tomography, Dartmouth College, in Hanover, New Hampshire, USA.
- [13] R. M. Brown and G. Uhlmann, *Uniqueness in the inverse conductivity problem for nonsmooth conductivities in two dimensions*, Comm. Partial Differential Equations, **22** (1997), 1009–1027.
- [14] A. P. Calderón, *On an inverse boundary value problem* Seminar on Numerical Analysis and its Applications to Continuum Physics, Soc. Brasileira de Matemática, 1980, 65–73.
- [15] M. Cheney and D. Isaacson, *Distinguishability in impedance imaging*, IEEE Trans. Biomed. Engr., **39** (1992), 852–860.
- [16] M. Cheney, D. Isaacson and J. C. Newell, *Electrical Impedance Tomography*, SIAM Review, **41** (1999), 85–101.
- [17] M. Cheney, D. Isaacson, J. Newell, J. Goble and S. Simske, *NOSER: An algorithm for solving the inverse conductivity problem*, Internat. J. Imaging Systems and Technology, **2** (1990), 66–75.
- [18] R. D. Cook, G. J. Saulnier and J. C. Goble, *A phase sensitive voltmeter for a high-speed, high-precision electrical impedance tomograph*, Annual International Conference of the IEEE Engineering in Medicine and Biology Society, **Vol.13, No.1** (1991), 22–23.
- [19] H. Cornean, K. Knudsen and S. Siltanen, *Towards a D-bar reconstruction method for three-dimensional EIT*, Journal of Inverse and Ill-posed Problems, **12** (2006), 111–134.
- [20] D. C. Dobson, *Convergence of a reconstruction method for the inverse conductivity problem*, SIAM J. Appl. Math., **52(2)** (1992), 442–458.
- [21] D. C. Dobson and F. Santosa, *An image-enhancement technique for electrical impedance tomography*, Inverse Problems, **10** (1994), 317–334.
- [22] M. Ikehata and S. Siltanen, *Numerical solution of the Cauchy problem for the stationary Schrödinger equation using Faddeev's Green function*, SIAM J. Appl. Math., **64** (2004), 1907–1932.
- [23] D. Isaacson, J. L. Mueller, J. C. Newell and S. Siltanen, *Reconstructions of chest phantoms by the D-bar method for electrical impedance tomography*, IEEE Trans. Med. Im., **23** (2004), 821–828.
- [24] D. Isaacson, J. L. Mueller, J. C. Newell and S. Siltanen, *Imaging cardiac activity by the D-bar method for electrical impedance tomography*, Physiol. Meas., **27** (2006), S43–S50.
- [25] J. Kaipio, V. Kolehmainen, E. Somersalo and M. Vauhkonen, *Statistical inversion and Monte Carlo sampling methods in electrical impedance tomography*, Inverse Problems, **16** (2000), 1487–1522.
- [26] S. Kindermann and A. Leitão, *Regularization by dynamic programming*, J. Inverse Ill-Posed Probl., **15 no. 3** (2007), 295–310.
- [27] K. Knudsen, *On the Inverse Conductivity Problem*, Ph.D. thesis, Department of Mathematical Sciences, Aalborg University, Denmark (2002)
- [28] K. Knudsen, *A new direct method for reconstructing isotropic conductivities in the plane*, Physiol. Meas., **24** (2003), 391–401.
- [29] K. Knudsen and A. Tamasan, *Reconstruction of less regular conductivities in the plane*, Comm. Partial Differential Equations, **29** (2004), 361–381.

- [30] K. Knudsen, J. L. Mueller and S. Siltanen, *Numerical solution method for the D-bar-equation in the plane*, J. Comp. Phys., **198** (2004), 500–517.
- [31] K. Knudsen, M. J. Lassas, J. L. Mueller and S. Siltanen, *D-bar method for electrical impedance tomography with discontinuous conductivities* SIAM J. Appl. Math., **67** (2007), 893–913.
- [32] K. Knudsen, M. Lassas, J. L. Mueller and S. Siltanen, *Reconstructions of piecewise constant conductivities by the D-bar method for Electrical Impedance Tomography*, Journal of Physics: Conference Series, **124** (2008),.
- [33] K. Knudsen, M. Lassas, J. L. Mueller and S. Siltanen, *Regularized D-bar method for the inverse conductivity problem*, Inverse Problems and Imaging, **3** (2009), 599–624.
- [34] V. Kolehmainen, M. Lassas and P. Ola, *The inverse conductivity problem with an imperfectly known boundary*, SIAM J. Appl. Math., **66** (2005), 365–383.
- [35] V. Kolehmainen, M. Lassas and P. Ola, *The inverse conductivity problem with an imperfectly known boundary and reconstruction up to a conformal deformation*,
- [36] V. Kolehmainen, M. Lassas and P. Ola, *Electrical Impedance Tomography Problem with Inaccurately Known Boundary and Contact Impedances*, IEEE Transactions on Medical Imaging, **27** (2008), 1404–1414.
- [37] A. Lechleiter and A. Rieder, *Newton regularizations for impedance tomography: a numerical study*, Inverse Problems, **22** (2006), 1967–1987.
- [38] J. L. Mueller and S. Siltanen, *Direct reconstructions of conductivities from boundary measurements*, SIAM J. Sci. Comp., **24** (2003), 1232–1266.
- [39] E. K. Murphy, *2-D D-bar Conductivity Reconstructions on Non-circular Domains*, Doctoral thesis, Colorado State University, 2007.
- [40] E. K. Murphy, J. L. Mueller and J. C. Newell, *Reconstructions of conductive and insulating targets using the D-bar method on an elliptical domain*, Physiol. Meas., **28** (2007), S101–S114.
- [41] A. I. Nachman, *Reconstructions from boundary measurements*, Ann. of Math., **128** (1988), 531–576.
- [42] A. I. Nachman, *Global uniqueness for a two-dimensional inverse boundary value problem*, Ann. of Math., **143** (1996), 71–96.
- [43] G. Nakamura, K. Tanuma, S. Siltanen and S. Wang, *Numerical recovery of conductivity at the boundary from the localized Dirichlet to Neumann map*, Computing, **75** (2005), 197–213.
- [44] R. G. Novikov, *A multidimensional inverse spectral problem for the equation  $-\Delta\psi + (v(x) - Eu(x))\psi = 0$* , Funktsional. Anal. i Prilozhen., **22** (1988), 11–22, (transl.) Funct. Anal. Appl., **22**, 263–272.
- [45] D. Roy, G. Nicholls and C. Fox, *Imaging convex quadrilateral inclusions in uniform conductors from electrical boundary measurements*, Stat Comput, **19** (2009), 17–26.
- [46] A. Seppänen, M. Vauhkonen, P. J. Vauhkonen, E. Somersalo and J. P. Kaipio, *State estimation with fluid dynamical evolution models in process tomography - an application to impedance tomography*, Inverse Problems, **17** (2001), 467–483.
- [47] H. Shan, M. V. Klibanov, H. Liu, N. Pantong and J. Su, 2008 *Numerical implementation of the convexification algorithm for an optical diffusion tomograph*, Inverse Problems, **24** (2008), 18 pp.
- [48] S. Siltanen, J. Mueller and D. Isaacson, *An implementation of the reconstruction algorithm of A. Nachman for the 2-D inverse conductivity problem*, Inverse Problems, **16** (2000), 681–699.
- [49] E. Somersalo, M. Cheney, D. Isaacson and E. Isaacson, *Layer stripping: a direct numerical method for impedance imaging*, Inverse Problems, **7** (1991), 899–926.
- [50] J. Sylvester, *A convergent layer stripping algorithm for the radially symmetric impedance tomography problem*, Communications in partial differential equations, **17** (1992), 1955–1994.
- [51] J. Sylvester and G. Uhlmann, *A global uniqueness theorem for an inverse boundary value problem*, Ann. of Math, **125** (1987), 153–169.

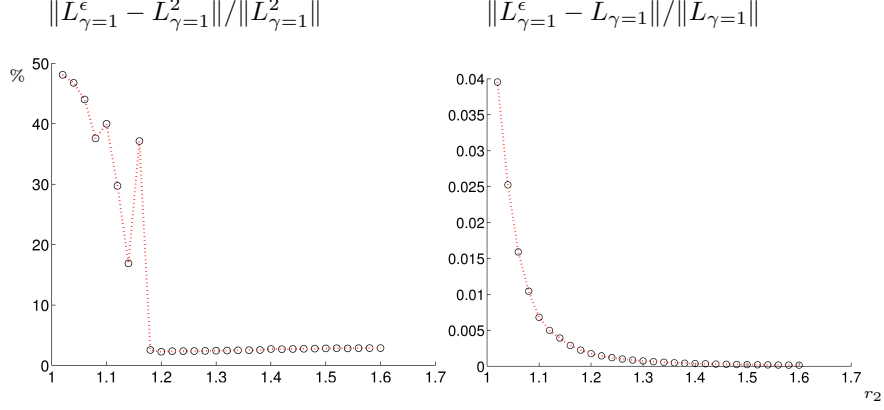


FIGURE 1. Left: relative error  $\|L_{\gamma=1}^\epsilon - L_{\gamma=1}^2\|/\|L_{\gamma=1}^2\|$  as a function of  $r_2$ . Here  $L_{\gamma=1}^\epsilon$  is the DN map on  $\partial\Omega_2$  computed from noisy ND map using formula (18) and  $L_{\gamma=1}^2$  is the DN map calculated directly on  $\partial\Omega_2$ . Here  $\|\cdot\|$  denotes the standard square norm for matrices. By  $\gamma = 1$  we mean  $\sigma = 1$  extended by (16). Right: relative error  $\|L_{\gamma=1}^\epsilon - L_{\gamma=1}\|/\|L_{\gamma=1}\|$  as a function of  $r_2$ . Here  $L_{\gamma=1}$  is the DN map computed from non-noisy ND map using formula (18).

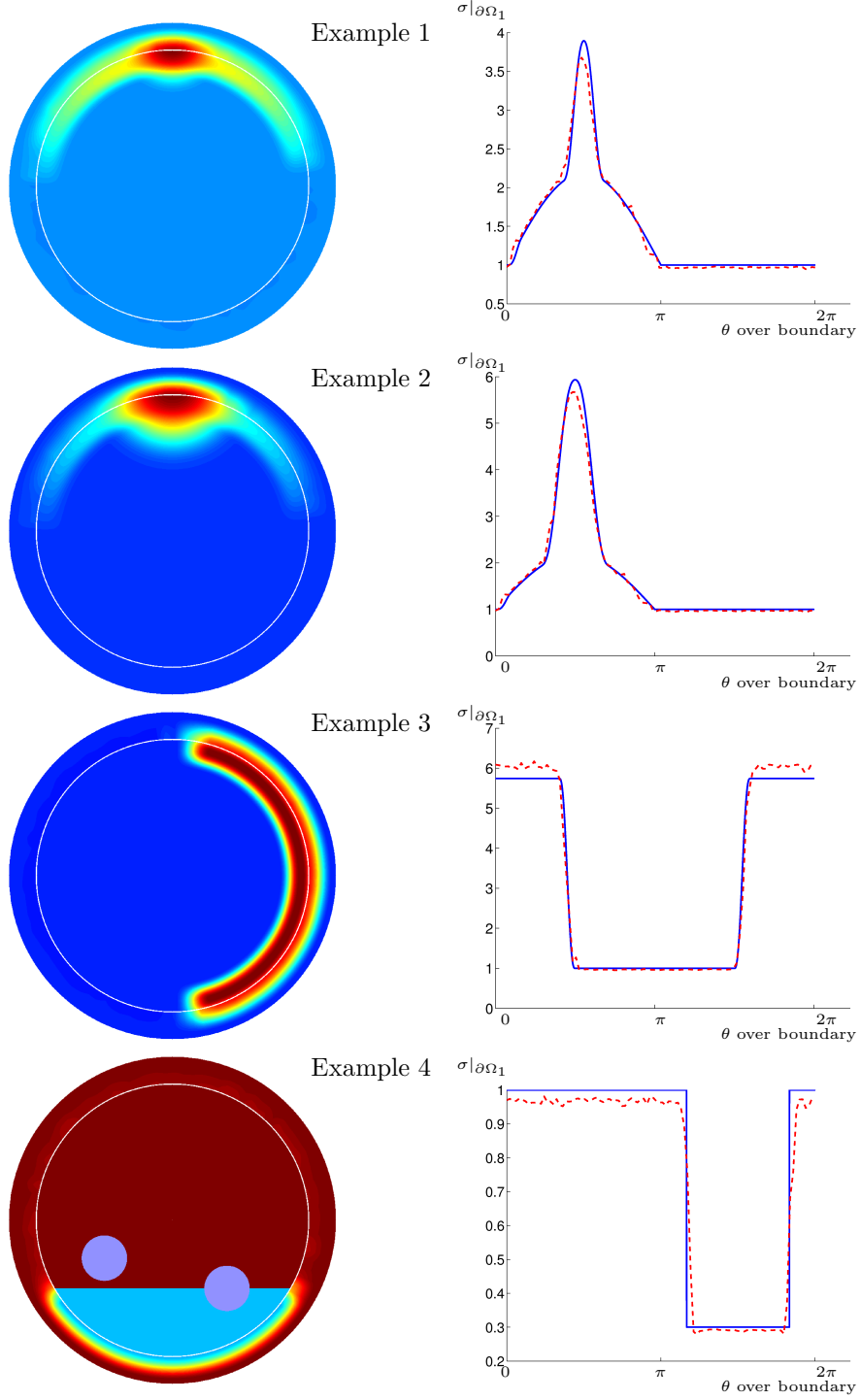


FIGURE 2. Left column: Example conductivities  $\gamma$  shown in the extended domain  $\Omega_2$ , the white circle indicates the inner boundary  $\partial\Omega_1$ . Right column: actual traces of the conductivities at the inner boundary  $\partial\Omega_1$  (solid line), and approximate traces at  $\partial\Omega_1$  (dashed line) whose reconstruction is explained in Section 3.

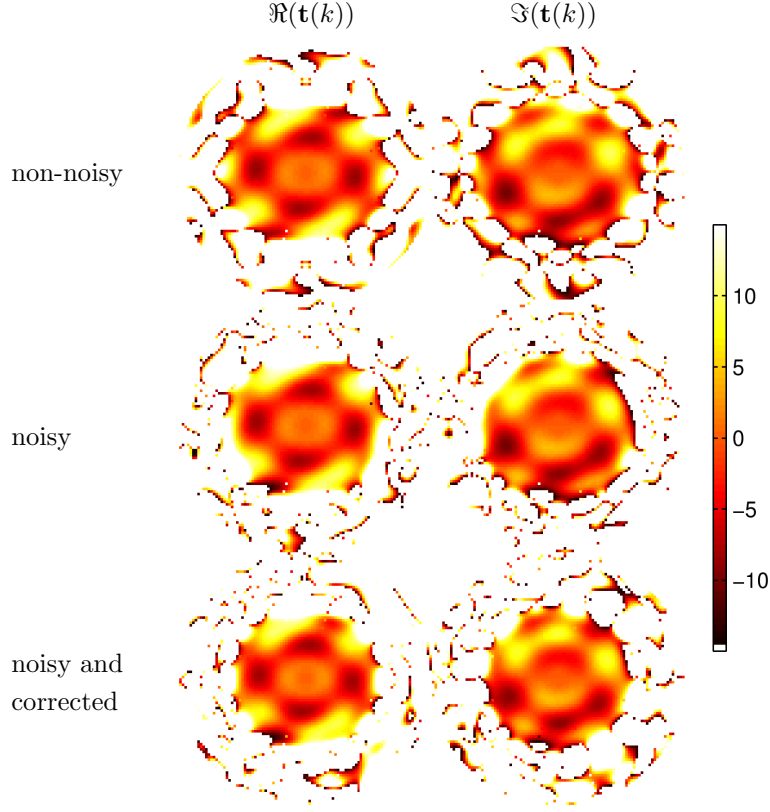


FIGURE 3. The scattering transform in example four. The first row shows the the real and imaginary parts of (23) substituting  $L_\sigma$  in place of  $\mathcal{L}_\sigma^\varepsilon$ . The second row shows the same functions using  $L_\sigma^\varepsilon$ , and the third row is again the same, but uses  $L_\gamma^\varepsilon$  calculated from (18). The real part of  $\mathbf{t}_R(k)$  is in the left column, the imaginary part on the right. The scattering transform is calculated in a grid of spectral parameters  $k$ , where  $|k| < 10$ . In white areas we have  $|\mathbf{t}_R(k)| > 15$ , meaning the calculation has failed or is close to failing due to computational error caused by large values of  $|k|$ .

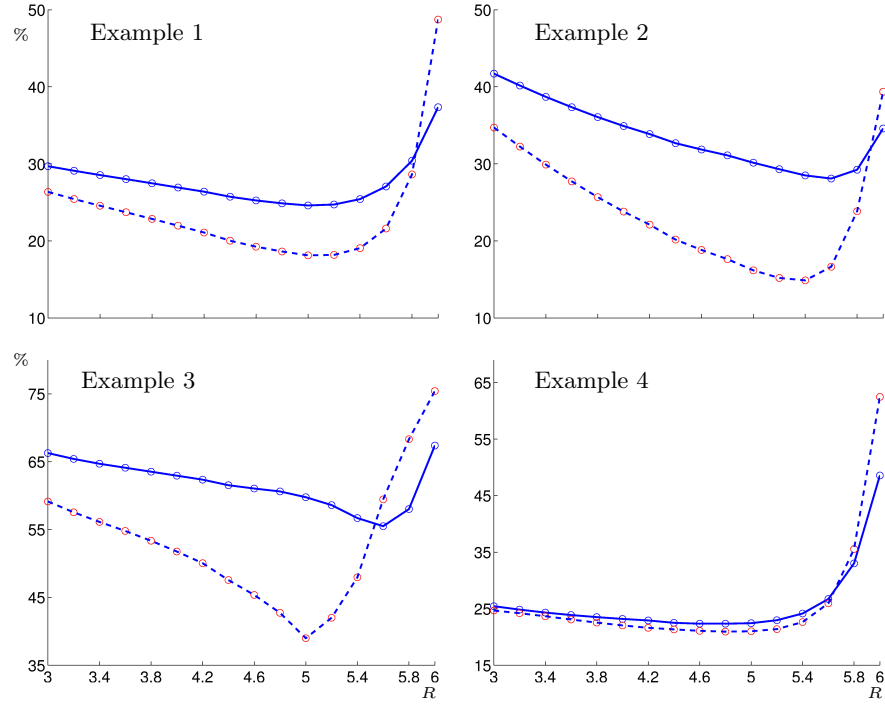


FIGURE 4.  $L^2$ -error graphs as a function of truncation radius  $R$  of the scattering transform for different examples; solid line is for the traditional D-bar reconstructions, dashed line is for boundary corrected reconstructions. The  $R$ -axis is the same in all four plots.

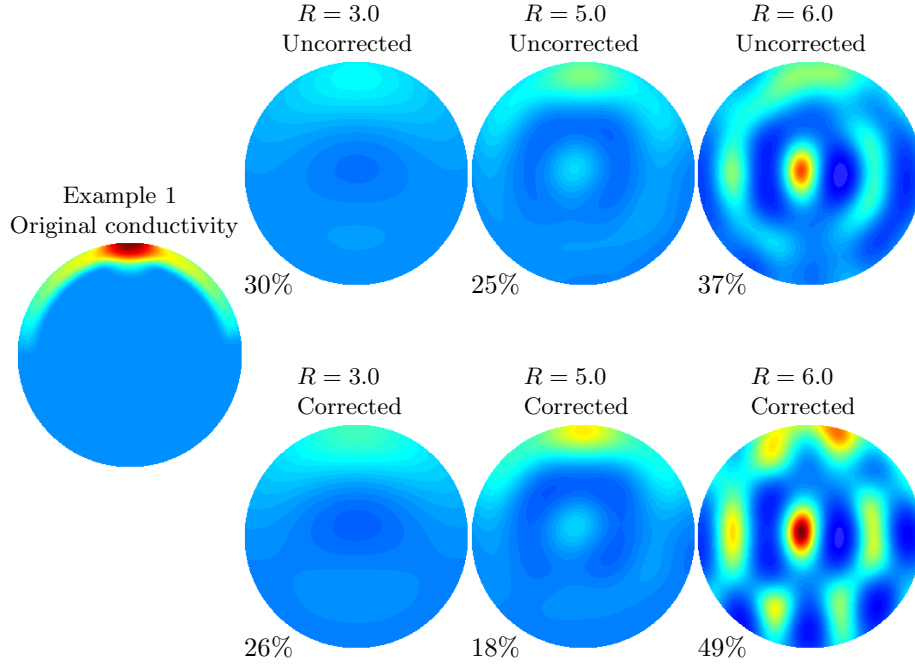


FIGURE 5. Example 1 reconstructions; the original conductivity on the left, traditional D-bar reconstructions on the upper row and boundary corrected reconstructions on the lower row; the numbers beside the pictures are  $L^2$ -errors, for the full error graph, see figure 4. The first reconstruction pair is always calculated with  $R = 3$ , the second one is the one with the lowest numerical  $\mathcal{L}^2$ -error for the boundary corrected reconstruction, and the third one is with  $R = 6$  to show how the reconstructions fail.

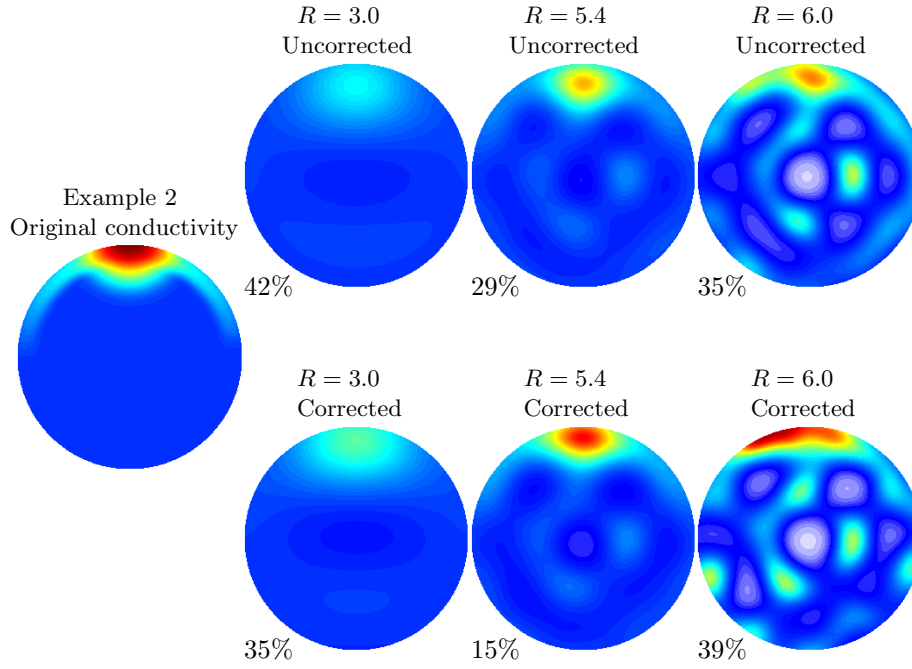


FIGURE 6. Example 2 reconstructions; the original conductivity on the left, traditional D-bar reconstructions on the upper row and boundary corrected reconstructions on the lower row; the numbers beside the pictures are  $L^2$ -errors, for the full error graph, see figure 4. The first reconstruction pair is always calculated with  $R = 3$ , the second one is the one with the lowest numerical  $\mathcal{L}^2$ -error for the boundary corrected reconstruction, and the third one is with  $R = 6$  to show how the reconstructions fail.

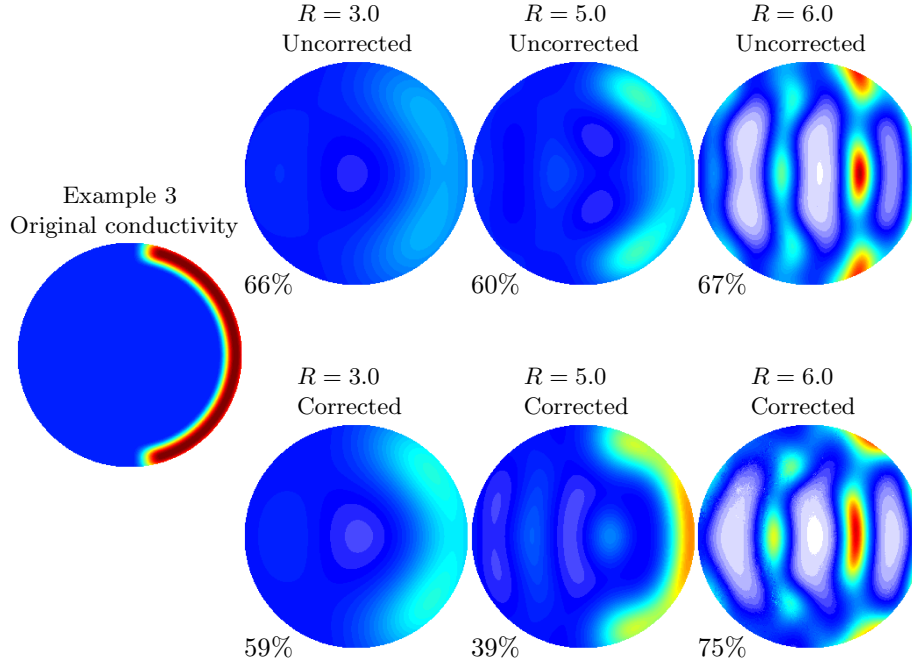


FIGURE 7. Example 3 reconstructions; the original conductivity on the left, traditional D-bar reconstructions on the upper row and boundary corrected reconstructions on the lower row; the numbers beside the pictures are  $L^2$ -errors, for the full error graph, see figure 4. The first reconstruction pair is always calculated with  $R = 3$ , the second one is the one with the lowest numerical  $\mathcal{L}^2$ -error for the boundary corrected reconstruction, and the third one is with  $R = 6$  to show how the reconstructions fail.

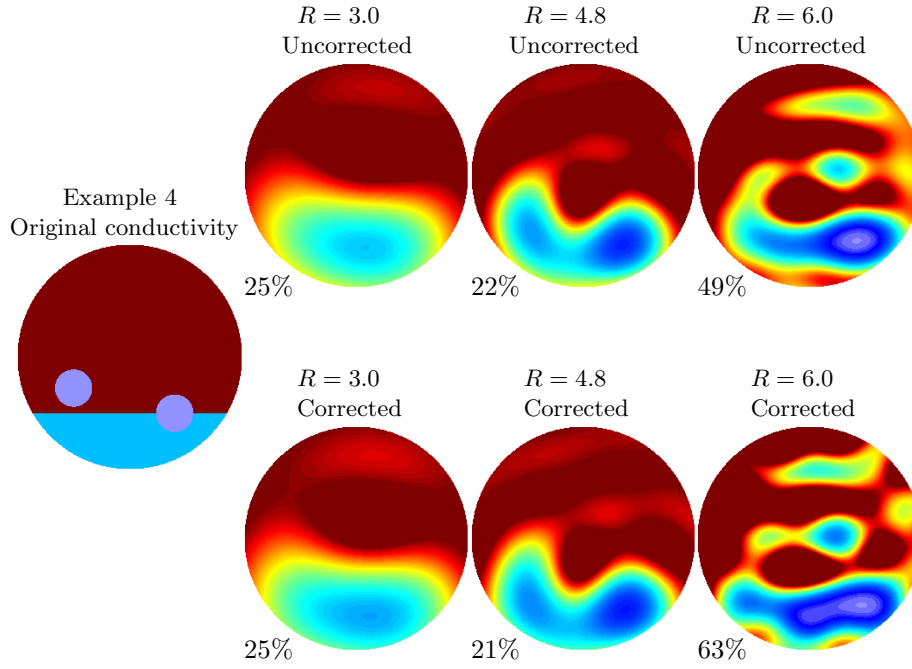


FIGURE 8. Example 4 reconstructions; the original conductivity on the left, traditional D-bar reconstructions on the upper row and boundary corrected reconstructions on the lower row; the numbers beside the pictures are  $L^2$ -errors, for the full error graph, see figure 4. The first reconstruction pair is always calculated with  $R = 3$ , the second one is the one with the lowest numerical  $\mathcal{L}^2$ -error for the boundary corrected reconstruction, and the third one is with  $R = 6$  to show how the reconstructions fail.